Biomedical Signal Processing and Control 80 (2023) 104354

Contents lists available at ScienceDirect

Biomedical Signal Processing and Control

journal homepage: www.elsevier.com/locate/bspc

Automatic algorithm for determining bone and soft-tissue factors in dual-energy subtraction chest radiography

Quan Do [a,*], Wontaek Seo [b], Choul Woo Shin [b]

[a] Department of Computer Science, UiT The Arctic University of Norway, 9037 Tromsø, Norway
[b] R&D Center, DRTECH Corporation, Gyeonggi-do, 13558 Seongnam-si, South Korea

ARTICLE INFO

Keywords:
Dual-energy subtraction
Medical image processing and analysis
Computer-aided diagnosis
Chest radiography
Lung cancer
Medical imaging

ABSTRACT

Lung cancer is currently the first leading cause of worldwide cancer deaths since the early stage of lung cancer detection is still a challenge. In lung diagnosis, nodules sometimes overlap with ribs and tissues on lung chest radiographic images, which are complex for doctors and radiologists. Dual-energy subtraction (DES) is a suitable solution to solve those issues. This article will develop an efficient iterative DES for lung chest radiographic images. Moreover, we propose an automatic algorithm for accurately determining bone and soft-tissue factors for subtraction. The proposed algorithm for determining the bone and soft-tissue factors is based on window/level ratio and radiographic histogram analysis. First, we take the image sampling from the original size 3072 × 3072 to 512 × 512 to reduce the processing time while achieving the bone and soft-tissue factors. Next, we compute the window/level ratio on the soft-tissue image. Finally, we determine the minimum value of the ratio to obtain the optimal soft-tissue and bone factors. Our experimental results show that our proposed algorithm achieves a minimized runtime of 200 ms, outperforming the GE algorithm's time of 4 s. The runtime of our DES of 6.066 s is shorter than the Fujifilm algorithm of 10 s while visualizing nodules on soft-tissue images and obtaining a similar quality of the soft-tissue images compared with the other algorithms. The academic contributions include the proposed algorithm for determining bone and soft-tissue factors and the optimized iterative DES algorithm to minimize time and dose consumption.

1. Introduction

According to the World Health Organization (WHO), lung cancer is currently the first leading cause of worldwide cancer deaths [1]. Lung cancer was also considered the second most common new cancer case in 2020. For this reason, the early stage of lung cancer detection is still a challenge. In lung diagnosis, nodules sometimes overlap with ribs and tissues on lung chest radiographic images [2–4]; hence, it is difficult for doctors and radiologists to have an exact diagnosis. Dual-energy subtraction (DES) is a suitable solution to solve that issue [5,6]. Another advantage of DES is to support radiologists in speeding up the reading of radiographic images [7,8].

Avinash et al. [9–11] used the difference in X-ray absorption characteristics to take DES images to obtain soft-tissue and bone images to solve the difficulty in diagnosis. To overcome dark soft-tissue images, the researchers searched bone and soft-tissue factors based on maximized salient bones. In that way, the researchers claimed that the bone and soft-tissue factors were optimal. With that solution, dose usage was 120% of the standard dose instead of double. However, there was a limitation of runtime in that method. That method detected the soft-tissue factor based on maximized salient bones with 25 steps on a 512 × 512 image in 4 s on a Sun Microsystems Ultra workstation.

Kashani et al. [12] used a subtraction technique similar to the research in [11], but the researchers used a manual DES factor detection such as a "two-slice volume". It may make a burden for radiologists and doctors to diagnose. However, that research demonstrated a performance advantage of DES imaging compared to traditional radiographic images.

Kawamura et al. [13] proposed another DES method. The researchers used an image registration for DES. With a multi-resolution technique, that method detected motion directions of the heartbeat, the breathing, and the movement of patients during two exposures, which caused misregistration artifacts on a subtracted image. As a result, that method reduced these misregistration artifacts. However, that method used an extended runtime of up to 10 s for the entire process on an Intel Core 2 Duo 3.0 GHz PC.

Fukao et al. [14] proposed a new filtering approach to reduce the dose for patients in the DES process. The researchers claimed that the dose usage was 150% of the standard dose instead of double. In that

* Corresponding author.
E-mail addresses: quan.do@uit.no (Q. Do), wtseo@drtech.co.kr (W. Seo), cwshin@drtech.co.kr (C.W. Shin).

https://doi.org/10.1016/j.bspc.2022.104354
Received 7 July 2022; Received in revised form 7 October 2022; Accepted 30 October 2022

method, the researchers used iterative filters such as a lowpass filter to reduce noise and a smoothing filter to separate the noise from the bone signal components in the bone image. However, that method had a long runtime for iterative DES since each DES should use different suitable bone and soft-tissue factors.

Several limitations are observed in these DES methods. First, since nodules in many lung diagnoses overlap with ribs and tissues on lung chest radiographic images, we need a DES solution to support doctors' and radiologists' exact diagnoses. Second, there is still a need for a simple algorithm to detect the bone and soft-tissue factors since the method proposed in [9–11] was too complex. Third, the runtimes for detecting the bone and soft-tissue factors and the entire DES process were long, i.e., 4 s for detecting the bone and soft-tissue factors [11], 10 s for the whole DES process [13], and the burden for radiologist workload by using the manual DES [12].

This article aims to solve all listed limitations of these DES methods by using our proposed algorithm based on window/level ratio and digital X-ray radiographic histogram analysis. Besides proposing an efficient algorithm for detecting the bone and soft-tissue factors in DES, we also developed a simplified DES process to minimize the runtime. The contributions of this article are summarized as follows:

- We propose an efficient algorithm for determining the bone and soft-tissue factors in DES with a minimized runtime of 200 ms.
- We develop a new DES method that simplifies the iterative filtering process with a shorter runtime of 6.066 s.
- With the simplified iterative DES, we minimize the dose to 130% of the standard dose while visualizing nodules and obtaining a similar quality of the soft-tissue images compared with the other algorithms.
- The academic contributions include the efficient proposed algorithm for determining the bone and soft-tissue factors and optimized iterative DES to minimize time and dose consumption.

The rest of this article is organized as follows. Section 2 presents related works, which include detecting bone and soft-tissue factors and iterative DES. Section 3 describes our proposed algorithms for determining bone and soft-tissue factors and simplified iterative DES. Section 4 presents experimental results and discusses image quality assessment, dose usage, runtime, image quality comparison, and future work. Section 5 concludes this article.

2. Related works

2.1. Detecting bone and soft-tissue factors

Using the difference in X-ray absorption characteristics, we subtract dual-energy images to obtain soft-tissue and bone images called power-image division [11].

$$I_S = \frac{I_H}{(I_L)^{k_S}}, \tag{1}$$

$$I_B = \frac{I_H}{(I_L)^{k_B}}, \tag{2}$$

$$k_B = \frac{k_S + 1}{2}, \tag{3}$$

where I_S, I_B, I_L, I_H are the soft-tissue, bone, low-energy, and high-energy images, respectively; k_S and k_B are the soft-tissue and bone factors. In DES, the bone and soft-tissue factors are two crucial parameters which significantly affect the quality of the soft-tissue and bone images. The bone and soft-tissue factors should be detected automatically in practical diagnosis.

DES aims to visualize nodules in the soft-tissue or bone images. There are several examples of the DES results of GE [15]. In addition, other DES results are presented by Fujifilm in [16], Shimadzu in [17], and Carestream in [18]. Nodules sometimes overlap ribs and tissues on lung chest radiographic images [15]; hence, it is difficult for doctors and radiologists to diagnose accurately without a DES solution.

To optimize the outputs of DES, we have several conditions, such as the maximized contrast noise ratio (CNR) and the selection of good pairs of low and high energies. To maximize CNR, we set up the X-ray tube so that the multiplication of high energy in kilovoltage peak (kVp) and milli-ampere-second (mAs) should be approximate or equal to that of low energy as follows:

$$(kVp.mA.s)_{High\_energy} \cong (kVp.mA.s)_{Low\_energy}, \tag{4}$$

where kVp, mA, and s are kilovoltage peak, milli-ampere, and second parameters, respectively, for setting the X-ray tube to take high and low energy images.

Suppose we apply Eqs. (1) and (2) to obtain the soft-tissue and bone images, the contrast of lung field in the soft-tissue image is dark and not good enough for diagnosis. That is the first challenge of the DES problem. In GE's research [11], the researchers proposed an automatic algorithm to search the bone and soft-tissue factors based on the maximized salient bones to overcome this challenge; however, it resulted in a long runtime that motivated us to create this article. With that solution, the dose usage was 120% of the standard dose instead of double [9].

The soft-tissue factor detection was very long in GE's research [11]. In addition, the entire process for registration, DES, and image contrast enhancement in Fujifilm's research [13] was also long for real-time healthcare applications. Hence, this article proposes an automatic algorithm for determining the bone and soft-tissue factors in DES, whose runtime is much shorter than GE's and Fujifilm's algorithms.

2.2. Iterative dual-energy subtraction

DES uses high and low-energy exposures. If we try to reduce doses, it causes image noise. We should optimize the exposure condition to reduce the patient dose and control the image noise. In addition, the noise in the high- and low-energy images is amplified by subtracting two images. In other words, the noise in the soft-tissue image is more significant than in the low and high-energy images. That noise was formulated in [14] as follows:

$$Noise_S = \sqrt{Noise_{H^*}^2 + Noise_L^2}, \tag{5}$$

where $Noise_S$, $Noise_{H^*}$, and $Noise_L$ are the noise levels in the subtracted image, in the high-energy image multiplied with the subtraction factor, and in the low-energy image, respectively.

In [14], the researchers used a low-pass filter to reduce the noise components. In addition, a smoothing filter separated the noise from the bone signal components in the bone image. Two types of filters were iterative until they obtained the final satisfied soft-tissue image. That was another solution to overcome the dark soft-tissue challenge.

The researchers used various bone and soft-tissue factors to take subtraction iteratively in that research. In that way, they had contrast enhancement and noise filtering for the results of DES. In addition, that solution used a 1.5 times dose of the plain chest. However, the runtime of Fujifilm's iterative DES was 10 s [13]. The runtime for DES was long, which was a limitation of that method.

Our article will simplify the iterative process of DES, which will optimize the number of filters and iterations. Using that way, we reduce the noise components and the runtime of the entire DES process.

3. Proposed algorithms

3.1. Proposed algorithm for determining bone and soft-tissue factors

In Section 2.1, we introduced DES using the power-image division. However, we can take logarithms for both sides of Eqs. (1) and (2)

to obtain the soft-tissue and bone images called logarithmic image subtraction as follows:

$$I_S = k_S.log\left(I_H\right) - log\left(I_L\right), \tag{6}$$

$$I_B = k_B.log\left(I_H\right) - log\left(I_L\right). \tag{7}$$

If we want to use the logarithmic image subtraction, we obtain a relationship of k_B and k_S for DES as follows:

$$k_B = \frac{k_S + 0.75}{2}. \tag{8}$$

Eq. (8) is not known from the literature, but it is our research finding for DES using the logarithmic image subtraction. Through this equation, we can obtain a bone factor k_B if we know the soft-tissue factor k_S.

We will develop a new efficient iterative DES using histogram information with optimal bone and soft-tissue factors. We can determine the anatomical position on the histogram [19,20], as shown in Fig. 1(a). This figure shows the histogram distribution of pixel values from an image plate. Since collimators limit a beam of X-rays, the collimated area has a minor intensity, which means it is close to 0 or the left-hand side of the image histogram. In contrast, the open area without collimators, anatomies of humans, or phantoms has the highest intensity and is on the right-hand side of the image histogram. Finally, anatomies lie in the middle area because they prevent little X-rays that reduce the intensity to more minor than the open area.

That distribution is not only suitable for the plate or phantom but also correct for actual human chest images, as an example shown in Fig. 1(b) and the histogram of that chest image in Fig. 1(c). On the human chest image in Fig. 1(b), the mean intensity of collimators (area I) is 250, the mean intensity of anatomy (area II) equals 300, and the mean intensity of open area (area III) is 9150. Those intensities show correctly on the histogram in Fig. 1(c). Hence, we have already proved that the histogram distribution of phantoms for different areas in Fig. 1(a) has the same distribution as the human chest image in Fig. 1(c).

Since our low and high-energy images have no collimator, we only control the "Open area" position. We propose an algorithm for determining the bone and soft-tissue factors based on the window/level ratio and the digital X-ray radiographic image histogram analysis. The proposed algorithm is presented in the following steps:

Step 1 is pre-processing. We take the image sampling from the original size 3072 × 3072 to 512 × 512. By sampling the smaller image size, we can reduce the processing time while achieving our goal of determining the bone and soft-tissue factors. We substitute k_S = 0.53 – 0.85 with step = 0.01 into Eq. (6). If k_S is outside the range, we may not obtain the soft-tissue image or cannot obtain the subtraction successfully. By choosing k_S, we determine a soft-tissue image I_S for each k_S. Then, we determine a histogram of each soft-tissue image.

Step 2: We propose and define *Wratio* (*W* – window/level) to control the quality of the anatomy area on the soft-tissue image as follows:

$$Wratio = \frac{W_{Frequency\_max}}{W_2 - W_1}, \tag{9}$$

where W_2, W_1, and $W_{Frequency\_max}$ are the maximum, minimum, and pixel values at the maximum intensity frequency, respectively, on the histogram of the soft-tissue image. Since we rarely use collimators for lung chest images, the $Wratio$ can help us control the anatomy area on the lung chest images. To simplify matters to understand, we can see Fig. 1(a) as an example; W_1 is the minimum intensity on the left-hand side of the figure, W_2 shows the maximum intensity on the right-hand side of the figure, and $W_{Frequency\_max}$ lies at the top of the curve at the 'Open area' of the figure.

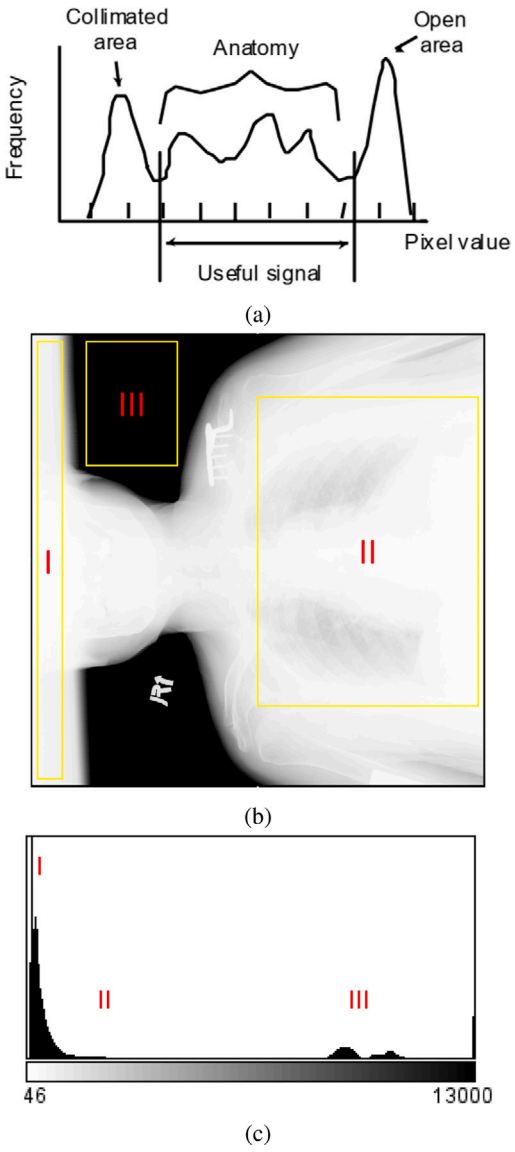

Fig. 1. Demonstration of histogram distribution of pixel values for (a) image plate (phantom) [19,20]. (b) Actual human chest image: the mean intensity of collimators (area I) is 250, the mean intensity of anatomy (area II) equals 300, and the mean intensity of open area (area III) is 9150. (c) Histogram of the human chest image in (b).

Step 3: We need the anatomy as visible as possible; hence, we need the minimum $Wratio$. That means we determine $Wratio_{min}$ to obtain the optimal k_S as follows:

$$k_{S_{opt}} = k_{S_{Wratio_{\min}}}. \tag{10}$$

To simplify matters to understand, we demonstrated two cases: single $Wratio_{min}$ and multiple $Wratio_{min}$ in Fig. 2. After obtaining $Wratio_{min}$, we get k_S of $Wratio_{min}$. That is the optimal k_S (abbreviation as $k_{S_{opt}}$).

The bone factor k_B is determined by Eq. (8). When $Wratio_{min}$ happens, we have maximized the anatomy area, which means the soft-tissue regions are the most apparent. That is also proper for the histogram distribution. In addition, when we have a single $Wratio_{min}$, k_S is the single minimum $Wratio$ point. When we have multi-$Wratio_{min}$, k_S is the average of multi-$Wratio_{min}$ points. We can sketch the relationship between $Wratio$ and k_S, as shown in Fig. 2.

We summarize our proposed algorithm for determining the bone and soft-tissue factors as presented in Fig. 3. Our proposed algorithm

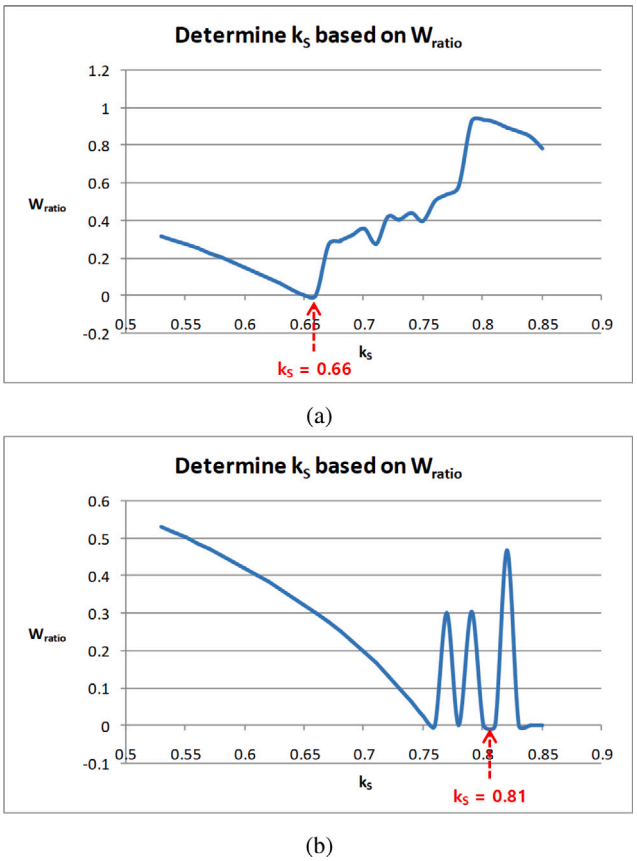

Fig. 2. Soft-tissue factor determination based on $Wratio_{min}$ for (a) single $Wratio_{min}$ and (b) multi-$Wratio_{min}$. The x coordinate indicates k_S – soft-tissue factor; the y coordinate presents $Wratio$ – window/level ratio.

is fast and straightforward for determining the bone and soft-tissue factors since we take the image sampling into the 512 × 512 matrix. We do not need to take segmentation and maximize the likelihood and the salient bones proposed in the GE's algorithm [11]. In addition, we only take three steps, such as preprocessing, computing $Wratio$, and obtaining $k_{S_{opt}}$, while the GE's algorithm takes 25 exhausting search steps. Hence, we can estimate that our proposed algorithm has a much shorter runtime than GE. This estimation is proved in our experimental results in Section 4.

3.2. Simplified iterative dual-energy subtraction

We will apply the previously mentioned bone and soft-tissue factors to a simplified iterative DES where all DES factors are optimal. The iterative DES algorithm is developed based on Fujifilm's algorithm for reducing the dose for patients [14]. Fig. 4 shows a flow chart of our iterative DES algorithm. In this figure, the symbol ⊖ presents DES, where we apply our proposed automatic algorithm for determining bone and soft-tissue factors in dual-energy subtraction chest radiography; the symbol ⊕ indicates blending dual-energy images.

Compared with the iterative DES method in [14], we do not use a lowpass filter for the soft-tissue images in our iterative DES algorithm. That means we reduce the number of filters to one for one DES process. In other words, the existing two filters and an iterative DES, which includes a smoothing filter, is redundant. The lowpass filter is used for the temporary soft-tissue image; we have a smoothing filter with a similar function for denoising. In addition, we have several iterations for several times of denoising. Finally, our experimental results in the next section will prove the efficiency of this simplification. By reducing

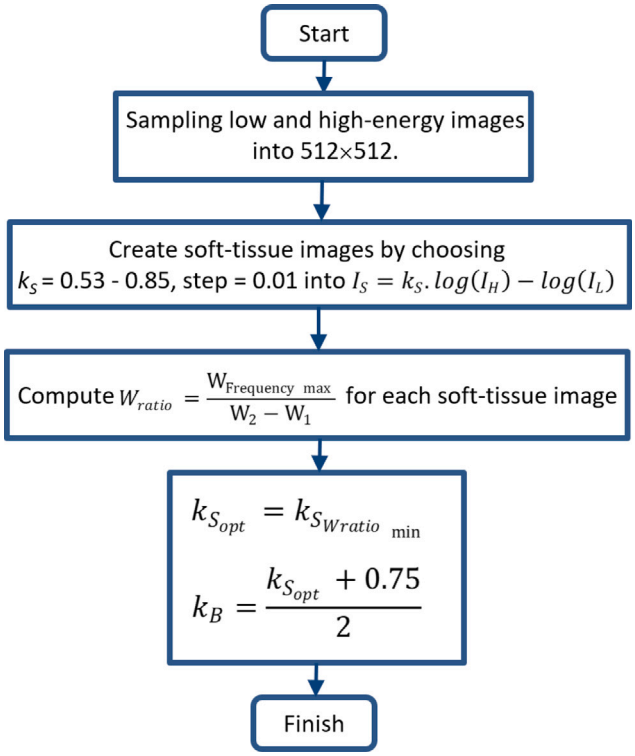

Fig. 3. Proposed algorithm for determining bone and soft-tissue factors. k_S – soft-tissue factor; k_B – bone factor; I_S – soft-tissue image; I_H – high-energy image; I_L – low-energy image; $Wratio$ – window/level ratio; W_2, W_1, and $W_{Frequency\_max}$ are the maximum, minimum, and pixel values at the maximum intensity frequency, respectively.

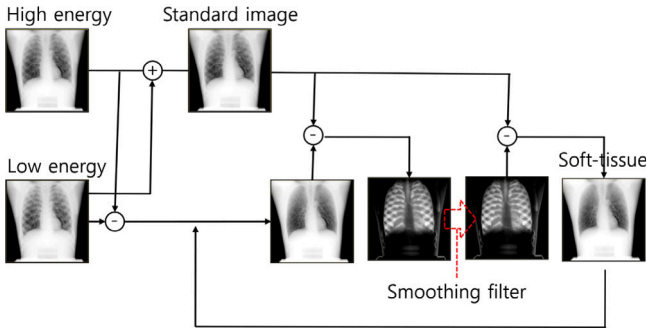

Fig. 4. Simplified iterative dual-energy subtraction (DES) algorithm. ⊕ indicates blending dual-energy images; ⊖ presents DES.

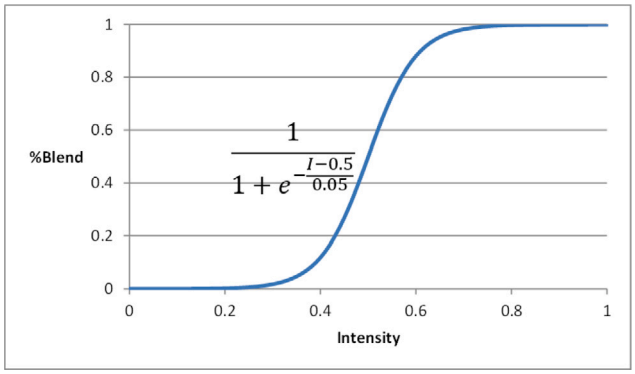

Fig. 5. Sigmoid curve for blending dual-energy images. I – input intensity applied sigmoid curve.

the number of filters, we simplify iterative DES, which makes our simplified iterative DES run faster than the original iterative DES of Fujifilm.

Since the iterative DES includes contrast enhancement and noise filtering, we use a sigmoid curve to blend dual-energy images to enhance the contrast of our simplified iterative DES. We blend dual-energy images as follows:

$$\%Blend_L = offset + \frac{1}{1 + e^{-\frac{I_L - c}{r}}}, \tag{11}$$

where $offset \in [0, 1]$, $\%Blend_L$ is a sigmoid function for enhancing the contrast of the low-energy image, I_L is the low-energy intensity, c is the center of the slope, and r is the rate of change in the transition from low to high. Fig. 5 is an example of a sigmoid curve for blending dual-energy images.

We use a sigmoid curve to enhance the contrast of dual-energy images. Using the sigmoid curve to blend dual-energy images is a lookup table (LUT) technique where the input image data are mapped to the output values, approximating the sigmoid function. The middle area of the sigmoid curve in Fig. 5 will effectively enhance the contrast of the central area of the input image's histogram (anatomy area) in Fig. 1(a). Finally, we combine low and high-energy images to make a standard image for enhancing contrast as follows:

$$I_{Standard} = \%Blend_L . I_L + \left(1 - \%Blend_L\right) . I_H. \tag{12}$$

Both our proposed algorithm for determining bone and soft-tissue factors and the simplified iterative DES algorithm are automatic and non-parametric. Our software program using these algorithms does not need any user interaction when it runs. Hence, our algorithms are practical and work well with all patients in clinical evaluations.

4. Experimental results and discussion

Experiments for this article were undertaken on a desktop with Intel Core i7-6700 3.4 GHz CPU, 16 GB RAM, and a 64-bit system. We implemented the proposed algorithms in C++. We tested on images of size 3072 × 3072 with two chest phantoms and nodules made by our radiologists. We are on developing steps and experimenting with phantoms in our laboratory. To avoid many X-ray doses on humans, using phantoms for research findings and constructing algorithms is the same as other companies, research institutes, and universities. In a similar work, GE's research was also performed using chest phantoms, i.e., in [9–11]. In addition, the producers tried to make chest phantoms similar to human chests. In some phantoms, the bones are human. We do not think there is much difference between phantoms and actual patients. Since X-rays can go through clothes, if the patients or phantoms do not keep metals, for example, lead, tungsten, etc., radiographic images of patients with clothes have no problems in clinical evaluations. We plan to extend clinical evaluations (trials) when we finish constructing the algorithms in our laboratory.

We experimented with 220 images in two datasets called 100 mA and 200 mA. We had 120 low and high-energy images for 100 mA and 100 low and high-energy images for 200 mA. We changed all possible parameters of the X-ray tube and combined the low and high-energy images: kVp step equals ten from 60 to 140, mA equals 100 or 200, and exposure time (s) equals 0.0063 to 0.1. Our radiologists have put all possible positions of nodules on the lung field and heart cages.

We have 9 variations of kVp and more than 50 variations of mAs with 100 mA. In addition, we have 6 variations of kVp and more than 50 variations of mAs with 200 mA. So that we have a total of 220 images and 77 DES images. GE's database in [11] has 6 variations of kVp and 4 variations of mAs, and Fujifilm's database in [13] has 31 DES images. Hence, our database is much more extensive than the two databases in all-level comparison. Our research topic in this article is DES, not machine learning or pattern recognition, which needs a lot of images in the database. In other words, our algorithms are not dependent on the number of images in the database. For the listed reasons, we conclude that our database is big enough to build and test the DES algorithms.

We will present the details of obtaining good-quality soft-tissue images to visualize nodules on lung chest images. We will then compare our results with GE's and Fujifilm's results regarding runtime, image quality, and dose usage. Finally, we will discuss our future work.

Table 1
Results of soft-tissue image assessment.

Contents	Terrible	Not accept	Accept	Good	Excellent
Amount	0	0	7	50	20
Percentage (%)	0%	0%	9.09%	64.94%	25.97%

4.1. Image quality assessment

We used a soft-tissue image to determine the nodules that result from our DES solution. We did not use a bone image for determining the nodules on a chest image, DES computed tomography (CT) with more dose-intensive and high-cost exams, rib suppression [21], and bone suppression using a single image in academic research [22–26] and medical industry [27–29]; hence, a discussion of the bone image [30], lung CT screening [31] or other unrelated subjects is out of the scope of this article.

We need human observation to observe image quality with small and detailed objects, such as soft tissues on chest radiographic images, since we have difficulty obtaining sample areas on the object and background to compute the contrast factor. Human being observation is still helpful for diagnosing as well as practical experiments. Our radiologists used the same criteria in [13] to determine the quality of the soft-tissue images, such as terrible, not accept, accept, good, and excellent. We took a similar evaluation as Fujifilm's research [13]. In addition, the judgment was undertaken by our well-trained radiologists. Hence, using the same criteria is fair for evaluation and comparison.

Fig. 6(a) presents the detailed criteria for the soft-tissue images. The different levels are based on contrast and artifacts in the soft-tissue images. The terrible case gives too much sharpness, remaining rib edges, and artifacts, so radiologists cannot diagnose. The unaccepted case shows remaining artifacts and rib edges to be hard to diagnose. The accepted case presents some rib edges; then diagnosing is possible. The good case shows good contrast and very few remaining rib edges. The excellent case offers perfect contrast, with no artifacts and remaining rib edges; hence, it is ideal for diagnosing.

The number of soft-tissue images is obtained by the condition defined in Eq. (4). The multiplication of the high energy in kVp and mAs should be approximate or equal to that of the low energy. If we choose the kVp and mAs, which are not satisfied this condition, or we choose a random k_S and k_B by a manual method, we may obtain a failed case as presented in Fig. 6(b). In the failed case, the ribs almost remained on the soft-tissue image.

We used several methods to reduce the rib edge artifacts, such as choosing a good mA and a suitable number of iterations. Between two datasets, 100 mA and 200 mA, we recognized a significant reduction of the rib edge artifacts using 100 mA, as shown in Fig. 6(c).

In addition, the number of iterations also affects the quality of the soft-tissue and bone images. We experimented with different iterations, i.e., no, one, and five. Finally, we obtained the best image quality with five iterations, as presented in Fig. 6(d).

We chose the best parameters, such as 100 mA and five iterations, to obtain the result. Fig. 7 shows an example of a soft-tissue image resulting from a combination of (60 kVp, 100 mA, 0.04 s) and (120 kVp, 100 mA, 0.025 s). Other soft-tissue images have a similar image quality. We used our proposed algorithm described in Section 3.1 and chose the best parameters, such as 100 mA and five iterations. Finally,

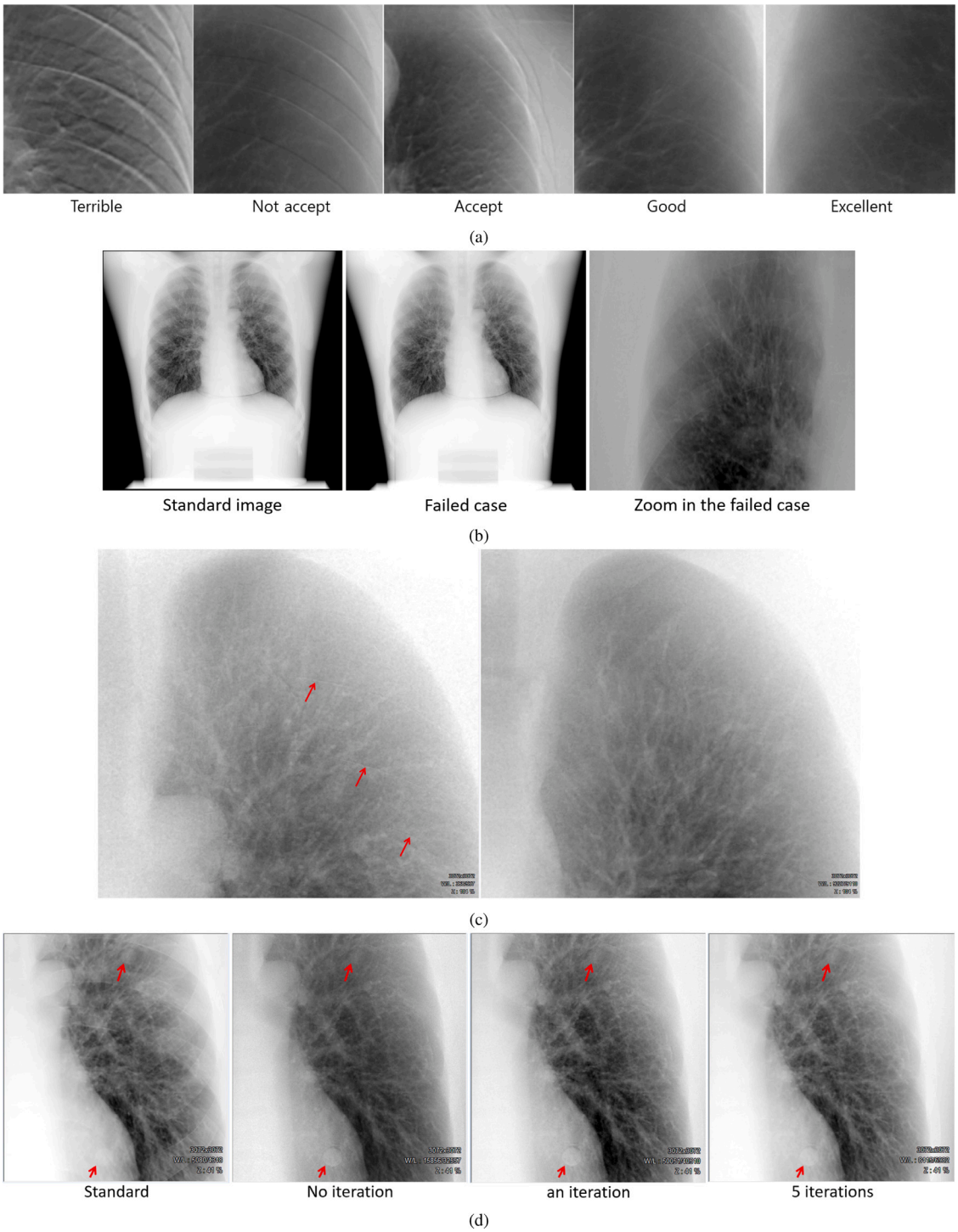

Fig. 6. Image quality optimization. (a) Criteria for quality assessment of soft-tissue images used the same criteria in [13]. (b) Failed case by choosing the wrong kVp and mAs. (c) Soft-tissue comparison between the left-hand side column: a combination of (80 kVp, 200 mA, 0.016 s) and (120 kVp, 200 mA, 0.008 s) and the right-hand side column: a combination of (60 kVp, 100 mA, 0.04 s) and (120 kVp, 100 mA, 0.032 s). Red arrows indicate rib-bone artifacts. (d) Soft-tissue comparison among various iterations. Red arrows indicate nodules on standard and soft-tissue images.

based on the criteria for soft-tissue images in Fig. 6(a), our radiologists assessed the quality of soft-tissue images, as presented in Table 1.

We tested two phantoms with 220 images scanned with all cases of doses and energies. We believe our algorithms will work well with all patients in clinical evaluations. To obtain a good-quality output image, a manual method for our algorithms, as shown in Fig. 4, is impossible or may get a failed case, as shown in Fig. 6(b).

After obtaining the soft-tissue images, as assessed in Table 1, we calculated our dose usage for DES as follows:

$$Dose_{DES} = mA_L.second_L + mA_H.second_H, \tag{13}$$

where $Dose_{DES}$ is the dose used in DES; mA_L and mA_H present mA for the low and high-energy images, respectively; $second_L$ and $second_H$ indicate the low and high-exposure time of digital flat-panel X-ray

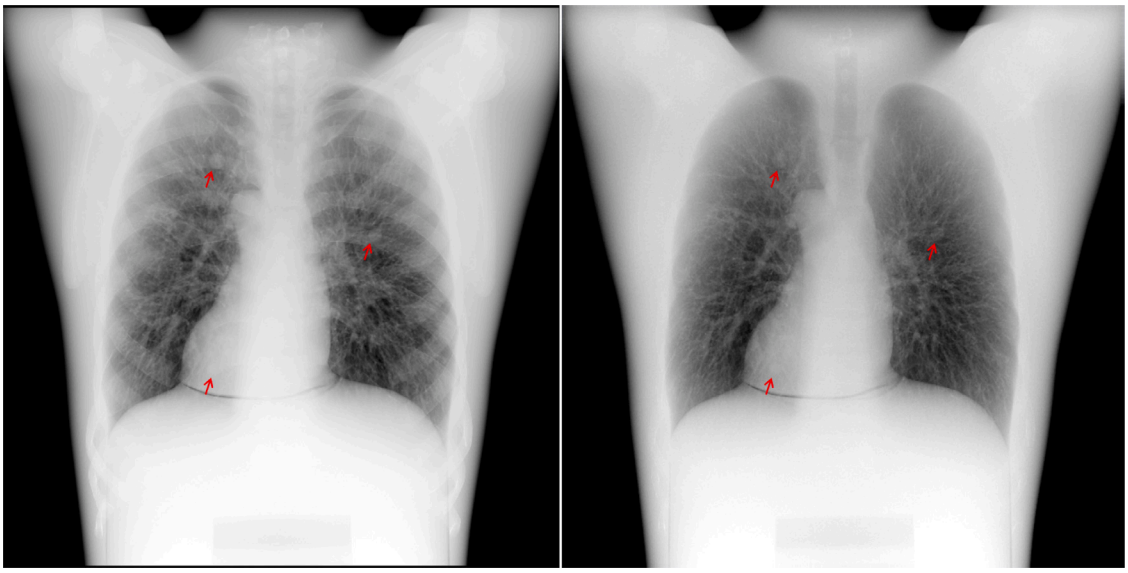

Fig. 7. An example of a soft-tissue image resulting from a combination of (60 kVp, 100 mA, 0.04 s) and (120 kVp, 100 mA, 0.025 s). The left-hand side is the standard image; the right-hand side is our soft-tissue image; the red arrows indicate nodules on standard and soft-tissue images.

Table 2
Runtime comparison among GE's, Fujifilm's, and our algorithms. NA — not applicable; DES — dual-energy subtraction. The bold underlining represents the best performance.

Contents	GE [11] (ms)	Fujifilm [13] (ms)	Ours (ms)
Factor detection	4000	NA	**200**
The entire DES	NA	10,000	**6066**

system for the low and high-energy images, respectively. For a normal chest, our radiologists used 5 mAs.

In the above example, we used a low-energy image (60 kVp, 100 mA, 0.04 s) and a high-energy image (120 kVp, 100 mA, 0.025 s), which means we had $Dose_{DES} = 6.5$ mAs $= 1.3 \times Dose_{normal\_chest}$. We used other similar doses for other DES images.

GE's method used 120% of the standard dose [9], and Fujifilm used 150% of the standard dose [14]. Our DES algorithm provides 130% of the standard dose, slightly better than Fujifilm. Hence, our proposed algorithm offers efficient dose usage.

4.2. Runtime comparison

We used five iterations for our iterative DES process to obtain the best image quality, as described in Section 4.1. As presented in Fig. 4, we only used our proposed algorithm to detect the bone and soft-tissue factors for the first stage; the other five iterative steps applied the fixed factors.

We tested 220 images and got 77 DES image pairs for our proposed algorithm for determining soft-tissue and bone factors and our simplified iterative DES. Table 2 shows the average runtime of our proposed algorithm compared to that of GE and Fujifilm algorithms. The runtime of our proposed algorithm for determining the bone and soft-tissue factors in 200 ms outperforms that of the GE's algorithm [11] in 4 s. In addition, the runtime of our iterative DES process in 6.066 s is shorter than that of the Fujifilm's algorithm [13] in 10 s.

4.3. Image quality comparison

Fig. 8 compares image quality among our DES, GE's [15], and Fujifilm's [16] results. The first and second columns in this figure present the standard and soft-tissue images, respectively. The red circles and red arrows show the nodules on the chest images. The primary purpose of DES is to remove ribs and bones to visualize nodules on soft-tissue images with no misregistration artifacts, no or less noise, and good contrast. The results of our image quality assessment are presented in Table 1 with the criteria shown in Fig. 6(a) and Section 4.1, which are the same criteria for the image quality assessment of Fujifilm's research in [13]. With the same criteria, we have a fair evaluation and comparison.

As shown in Fig. 8(a), a nodule overlaps with ribs and tissues on the lung chest radiographic image. Hence, it is difficult for doctors and radiologists to have an exact diagnosis if there is no DES solution. As we can see in this figure, the GE's result visualizes the nodule well. In addition, it shows no remained rib edges, no misregistration artifacts, no noise, and a good contrast between the lung fields and other anatomies.

Fig. 8(b) presents Fujifilm's results. There is no nodule on the chest image, and there are remaining blur clavicle bones and a few rib edges on DES's result. In addition, tissues on the lung field are slightly over-contrast compared with the first column's original chest image.

Fig. 8(c) shows our results. There are two nodules on this chest image: one in the middle of the lung field and another on the left ventricle. The right column of this image visualizes the nodules well, especially the nodule on the left ventricle. There are no artifacts, noise, and remaining rib bones, clavicles, or edges on our DES results. In addition, the figure shows that the contrast of the DES result is similar to the original contrast of the standard image on the left column.

Some background patterns exist since our radiologists did not make perfect offset and gain calibrations for the digital flat-panel X-ray detector when we experimented in our laboratory. After running through our iterative DES process with contrast enhancement, some combination doses of DES appeared patterns on the only background, not on the chest; hence, these patterns did not affect our image evaluation. We can refer to Fig. 7 without background patterns to confirm our explanation.

Our DES results visualize the nodules well from this discussion while retaining a similar contrast to the standard image. Compared with the GE's and Fujifilm's results, our result shows identical image quality in visualizing nodules on the chest image, good contrast on the lung field, and a similar contrast to the standard image. Other images in [15,16], and our results have a similar image quality comparison. This comparison shows that the image quality of our algorithm results is similar to or a little better than the other algorithms.

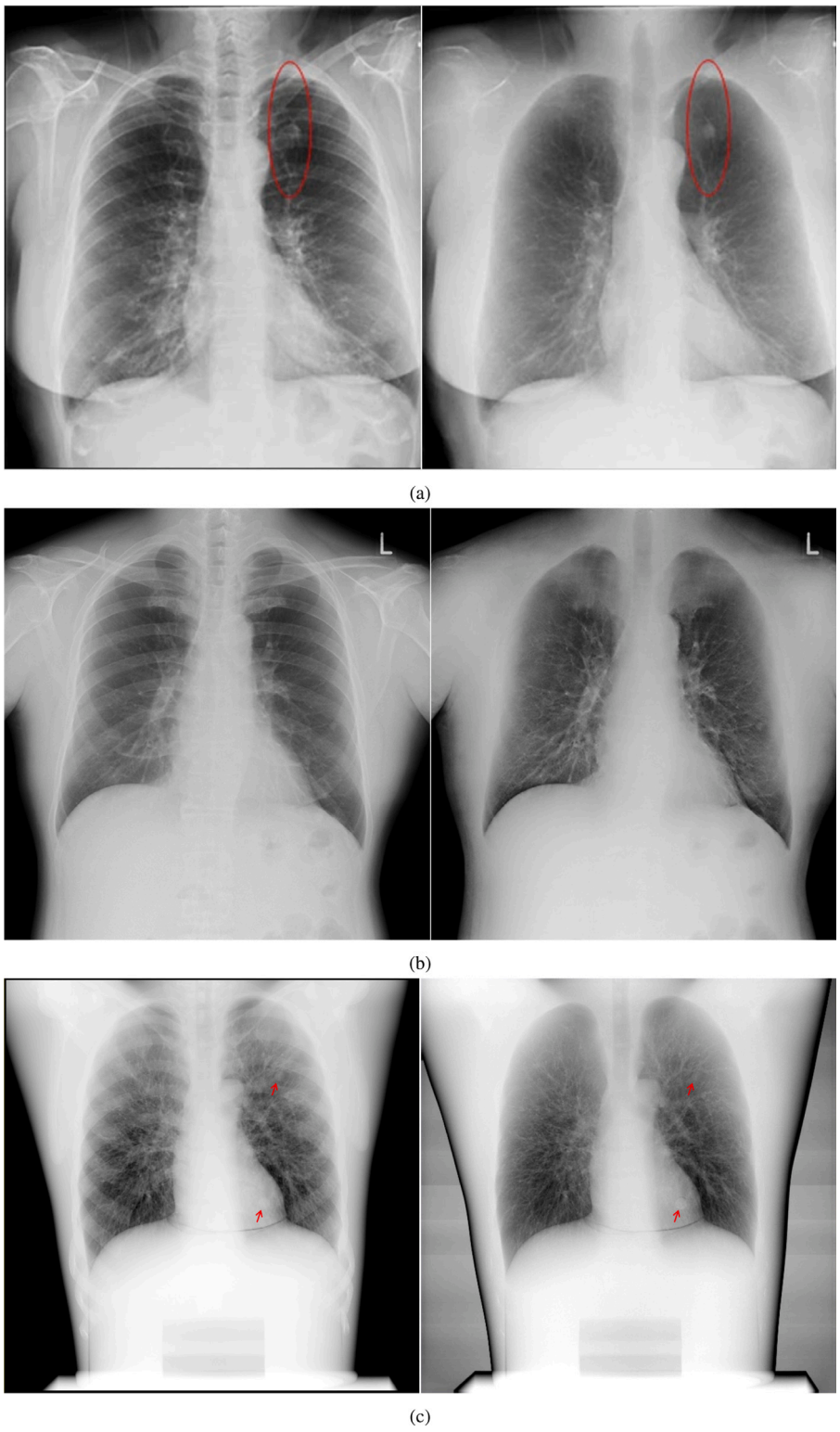

Fig. 8. Comparison of image quality among (a) GE's result [15], (b) Fujifilm's result [16], and (c) our result. The first and second columns present standard and soft-tissue images, respectively. Red circles and red arrows show nodules on chest images.

Finally, we have reviewed all product-level algorithms, such as GE's algorithm for detecting bone and soft-tissue factors and Fujifilm's algorithm for the entire process of DES, and compared those regarding dose usage, runtime, and image quality as described in the above sections. If we find any more high-quality DES algorithms, we will reach them.

4.4. Future work

We have already presented our efficient proposed algorithm for determining the bone and soft-tissue factors in DES using the window/level ratio and the digital X-ray radiographic histogram analysis. We have optimized our iterative DES to minimize time and dose consumption. Those are the academic contributions of this article.

We have three directions for our future work. They include: (a) reducing runtime using parallel processing, (b) using deep learning for automatically detecting nodules, and (c) reducing dose usage using state-of-the-art image processing techniques.

The runtime of the entire DES process is a limitation of our algorithms since we did not apply parallel processing in those algorithms. In future work, to reduce the runtime, we will use the latest high-performance computing, parallel processing, and optimization techniques for large matrix computation, i.e., 3072 × 3072 matrix. Those techniques are Intel Threading Building Blocks (TBB) and C Basic Linear Algebra Subprograms (CBLAS), which belong to the Intel Math Kernel Library (MKL) for large matrix computation, and programming optimization in C++. Those techniques have been applied successfully with an efficiency of 94.88% for reducing runtime [32]. By those techniques, we expect the runtime will be significantly reduced when running all processes, including determining the bone and soft-tissue factors, DES, the registration, and the enhancement of soft-tissue image contrast.

When we finish reducing the runtime of the entire DES using high-performance computing, parallel processing, and optimization techniques for large matrix computation, we will apply deep learning to detect nodules in soft-tissue images [26,33]. That work has a high chance of success since deep learning performance is now good enough in clinical evaluations.

Using our proposed algorithms, we obtained 130% of the standard dose, as described in Section 4.1, which is better than Fujifilm's result of 150% [14] but worse than GE's result of 120% [9]. That means we have room for improvement in the future. We may achieve our goal by using low-quality images of low doses and an automatic contrast enhancement technology [34] for subtracting dual-energy images.

5. Conclusion

This article proposes an automatic algorithm for determining the bone and soft-tissue factors in DES. Our proposed algorithm has minimized the runtime to 200 ms through our experimental results, much shorter than the GE algorithm's runtime of 4 s. Our iterative DES's runtime of 6.066 s also outperforms the Fujifilm algorithm's runtime of 10 s. With those results, our proposed algorithm is simplified. Simultaneously, we have achieved a similar image quality on the soft-tissue images compared with the other algorithms to visualize the nodules. Using our iterative DES algorithm, we got efficient dose usage, 130% of the standard dose, and the optimized runtime in the entire DES process.

Further work must be performed using the latest high-performance computing, parallel processing, and optimization techniques for large matrix computation. We expect to reduce the entire DES process's runtime significantly. In addition, we will consider applying deep learning to detect nodules in clinical evaluations and applying the latest contrast enhancement technology to reduce dose usage.

Declaration of competing interest

The authors declare that they have no known competing financial interests or personal relationships that could have appeared to influence the work reported in this paper.

Data availability

The authors do not have permission to share data.

Acknowledgments

The open-access publication charges for this article have been funded by a Grant from the publication fund of UiT The Arctic University of Norway. We thank senior radiologists Nam Jin Lee and Yong Ju Na for acquiring radiographic images and evaluating the quality of DES images. We would like to thank Editor-in-chief Professor Filippo Molinari and Scientific Managing Editor Banu Bayram for suggesting our manuscript submitted to the Biomedical Signal Processing and Control. We also appreciate the anonymous reviewers for their insightful and constructive comments and suggestions to make our manuscript more complete.

References

[1] WHO, Cancer, 2022, [Online]. Available: https://www.who.int/news-room/fact-sheets/detail/cancer, accessed: November 8th, 2022.

[2] A.M. Schilham, B. Van Ginneken, M. Loog, A computer-aided diagnosis system for detection of lung nodules in chest radiographs with an evaluation on a public database, Med. Image Anal. 10 (2) (2006) 247–258, http://dx.doi.org/10.1016/j.media.2005.09.003.

[3] M. Woźniak, D. Połap, G. Capizzi, G.L. Sciuto, L. Kośmider, K. Frankiewicz, Small lung nodules detection based on local variance analysis and probabilistic neural network, Comput. Methods Programs Biomed. 161 (2018) 173–180, http://dx.doi.org/10.1016/j.cmpb.2018.04.025.

[4] Y. Kimori, A morphological image processing method to improve the visibility of pulmonary nodules on chest radiographic images, Biomed. Signal Process. Control 57 (2020) 101744, http://dx.doi.org/10.1016/j.bspc.2019.101744.

[5] H. Tagashira, K. Arakawa, M. Yoshimoto, T. Mochizuki, K. Murase, Detectability of lung nodules using flat panel detector with dual energy subtraction by two shot method: evaluation by ROC method, Eur. J. Radiol. 64 (2) (2007) 279–284, http://dx.doi.org/10.1016/j.ejrad.2007.02.029.

[6] P. Vock, Z. Szucs-Farkas, Dual energy subtraction: principles and clinical applications, Eur. J. Radiol. 72 (2) (2009) 231–237, http://dx.doi.org/10.1016/j.ejrad.2009.03.046.

[7] F. Manji, J. Wang, G. Norman, Z. Wang, D. Koff, Comparison of dual energy subtraction chest radiography and traditional chest X-rays in the detection of pulmonary nodules, Quant. Imaging Med. Surg. 6 (1) (2016) 1, http://dx.doi.org/10.3978/j.issn.2223-4292.2015.10.09.

[8] Y. Liu, W. Yang, G. She, L. Zhong, Z. Yun, Y. Chen, N. Zhang, L. Hao, Z. Lu, Q. Feng, et al., Soft tissue/bone decomposition of conventional chest radiographs using nonparametric image priors, Appl. Bionics Biomech. 2019 (2019) http://dx.doi.org/10.1155/2019/9806464.

[9] G.B. Avinash, K.N. Jabri, R. Uppaluri, A. Rader, F. Fischbach, J. Ricke, U. Teichgraeber, Effective dose reduction in dual-energy flat panel X-ray imaging: technique and clinical evaluation, in: Medical Imaging 2002: Image Processing, Vol. 4684, SPIE, 2002, pp. 1048–1059, http://dx.doi.org/10.1117/12.467060.

[10] G.B. Avinash, J.M. Sabol, F.S. Nicolas, Method and apparatus to automatically determine tissue cancellation parameters in X-ray dual energy imaging, 2005, pp. 1–14, US Patent 6, 917, 697 B2. https://patents.google.com/patent/US6917697B2/en.

[11] J.M. Sabol, G.B. Avinash, Novel method for automated determination of the cancellation parameter in dual-energy imaging: evaluation using anthropomorphic phantom images, in: Medical Imaging 2003: Physics of Medical Imaging, Vol. 5030, International Society for Optics and Photonics, 2003, pp. 885–895, http://dx.doi.org/10.1117/12.480195.

[12] H. Kashani, J.G. Gang, N.A. Shkumat, C.A. Varon, J. Yorkston, R. Van Metter, N.S. Paul, J.H. Siewerdsen, Development of a high-performance dual-energy chest imaging system: initial investigation of diagnostic performance, Acad. Radiol. 16 (4) (2009) 464–476, http://dx.doi.org/10.1016/j.acra.2008.09.016.

[13] T. Kawamura, N. Omae, M. Yamada, W. Ito, K. Kawamoto, T. Doi, Image registration method based on multiresolution for dual-energy subtraction radiography, in: Medical Imaging 2012: Image Processing, Vol. 8314, International Society for Optics and Photonics, 2012, pp. 83141S1–83141S8, http://dx.doi.org/10.1117/12.910885.

[14] M. Fukao, K. Kawamoto, H. Matsuzawa, O. Honda, T. Iwaki, et al., Reduction of the dose to patients in dual-energy subtraction imaging of the chest with a direct-conversion flat panel detector (FPD) system, in: European Congress of Radiology-ECR 2010, 2010, pp. 1–21, http://dx.doi.org/10.1594/ecr2010/C-3292.

[15] GE, Dual energy subtraction, 2022, [Online]. Available: https://www.gehealthcare.com/products/radiography/advanced-applications/dual-energy-subtraction, accessed: November 8th, 2022.

[16] Fujifilm, Dual energy subtraction images, 2022, [Online]. Available: https://healthcaresolutions-us.fujifilm.com/digital-radiography/dr-rooms/fdr-visionary-suite#images, accessed: November 8th, 2022.

[17] Shimadzu, Dual energy subtraction, 2022, [Online]. Available: https://www.shimadzu-medical.eu/dual-energy-subtraction, accessed: November 8th, 2022.
[18] Carestream, Carestream's dose efficient dual energy imaging, 2022, [Online]. Available: https://www.youtube.com/watch?v=tDWCvgtoHgk, accessed: November 8th, 2022.
[19] J.A. Seibert, Physics of computed radiography: Overview of acceptance testing and quality control, AAPM (1999) 1–12, https://www.aapm.org/meetings/2001AM/pdf/7235-93936.pdf.
[20] R.A. Davidson, Radiographic Contrast-Enhancement Masks in Digital Radiography (Ph.D. thesis), The University of Sydney, 2006-01-01, http://hdl.handle.net/2123/1932.
[21] Y. Liu, X. Zhang, G. Cai, Y. Chen, Z. Yun, Q. Feng, W. Yang, Automatic delineation of ribs and clavicles in chest radiographs using fully convolutional DenseNets, Comput. Methods Programs Biomed. 180 (2019) 105014, http://dx.doi.org/10.1016/j.cmpb.2019.105014.
[22] M. Loog, B. van Ginneken, A.M. Schilham, Filter learning: application to suppression of bony structures from chest radiographs, Med. Image Anal. 10 (6) (2006) 826–840, http://dx.doi.org/10.1016/j.media.2006.06.002.
[23] S. Schalekamp, B. van Ginneken, L. Meiss, L. Peters-Bax, L.G. Quekel, M.M. Snoeren, A.M. Tiehuis, R. Wittenberg, N. Karssemeijer, C.M. Schaefer-Prokop, Bone suppressed images improve radiologists' detection performance for pulmonary nodules in chest radiographs, Eur. J. Radiol. 82 (12) (2013) 2399–2405, http://dx.doi.org/10.1016/j.ejrad.2013.09.016.
[24] W. Yang, Y. Chen, Y. Liu, L. Zhong, G. Qin, Z. Lu, Q. Feng, W. Chen, Cascade of multi-scale convolutional neural networks for bone suppression of chest radiographs in gradient domain, Med. Image Anal. 35 (2017) 421–433, http://dx.doi.org/10.1016/j.media.2016.08.004.
[25] L. Han, Y. Lyu, C. Peng, S.K. Zhou, GAN-based disentanglement learning for chest X-ray rib suppression, Med. Image Anal. 7 (2022) 1–14, http://dx.doi.org/10.1016/j.media.2022.102369.
[26] K. Cho, J. Seo, S. Kyung, M. Kim, G.-S. Hong, N. Kim, Bone suppression on pediatric chest radiographs via a deep learning-based cascade model, Comput. Methods Programs Biomed. 215 (2022) 106627, http://dx.doi.org/10.1016/j.cmpb.2022.106627.
[27] Carestream, Bone Suppression for Chest Radiographic Images, White Paper, Carestream Bone Suppression Software, 2014, pp. 1–6, [Online]. Available: https://www.carestream.com/en/us/medical/software/~/media//publicSite/Resources/Radiography%20and%20Health%20IT/Published%20Articles%20and%20White%20Papers/Image%20Capture/white-paper-bone-suppression-chest-201403.pdf.
[28] Riverain Technologies, Bone suppression, 2022, [Online]. Available: https://www.riveraintech.com/clearread-ai-solutions/clearread-xray/, accessed: November 8th, 2022.
[29] Philips, Philips bone suppression (by Riverain Technologies), 2022, [Online]. Available: https://www.philips.no/healthcare/resources/landing/bone-suppression, accessed: November 8th, 2022.
[30] Z. Szucs-Farkas, K. Lautenschlager, P.M. Flach, D. Ott, T. Strautz, P. Vock, T.D. Ruder, Bone images from dual-energy subtraction chest radiography in the detection of rib fractures, Eur. J. Radiol. 79 (2) (2011) e28–e32, http://dx.doi.org/10.1016/j.ejrad.2010.01.016.
[31] M. Sharma, M.S. Sandhu, U. Gorsi, D. Gupta, N. Khandelwal, Role of digital tomosynthesis and dual energy subtraction digital radiography in detection of parenchymal lesions in active pulmonary tuberculosis, Eur. J. Radiol. 84 (9) (2015) 1820–1827, http://dx.doi.org/10.1016/j.ejrad.2015.05.031.
[32] Q. Do, S. Acuña, J.I. Kristiansen, K. Agarwal, P.H. Ha, Highly efficient and scalable framework for high-speed super-resolution microscopy, IEEE Access 9 (2021) 97053–97067, http://dx.doi.org/10.1109/ACCESS.2021.3094840.
[33] C. Qin, D. Yao, Y. Shi, Z. Song, Computer-aided detection in chest radiography based on artificial intelligence: a survey, Biomed. Eng. Online 17 (1) (2018) 1–23, http://dx.doi.org/10.1186/s12938-018-0544-y.
[34] K. Gu, G. Zhai, X. Yang, W. Zhang, C.W. Chen, Automatic contrast enhancement technology with saliency preservation, IEEE Trans. Circuits Syst. Video Technol. 25 (9) (2014) 1480–1494, http://dx.doi.org/10.1109/TCSVT.2014.2372392.